Temporal dynamics of IR-to-visible up-conversion in $LiNbO_3$:Er^{3+}/Yb^{3+}: a path to phosphors with tunable chromaticity

Martina Marin-Dobrincic,[*] **Eugenio Cantelar, and Fernando Cusso**

Departamento Física de Materiales C-04, Universidad Autónoma de Madrid, 28049 – Madrid, Spain
[*]martina.dobrincic@uam.es

Abstract: In this work, a study of the temporal dynamical behavior of IR-visible up-conversion in the $LiNbO_3$: Er^{3+}/Yb^{3+} system under modulated IR excitation at 980 nm is presented. It is shown that modulation characteristics, including the relative green-to-red emission ratio (GRR), can be quantitatively explained by using the rate equations formalism. The relevant spectroscopic magnitudes are identified and this provides a general framework to explore the properties of other Er^{3+}/Yb^{3+} doped up-converting phosphors.

©2012 Optical Society of America

OCIS codes: (160.2540) Fluorescent and luminescent materials; (160.3730) Lithium niobate; (160.5690) Rare-earth-doped materials; (300.6280) Spectroscopy, fluorescence and luminescence; (250.5230) Photoluminescence.

References and links

1. N. Tansu, J. Y. Yeh, and L. J. Mawst, "Extremely-low threshold-current-density InGaAs quantum well lasers with emission wavelength of 1215-1233 nm," Appl. Phys. Lett. **82**(23), 4038–4040 (2003).
2. T. Takeuchi, Y.-L. Chang, A. Tandon, D. Bour, S. Corzine, R. Twist, M. Tan, and H.-C. Luan, "Low threshold 1.2 µm InGaAs quantum well lasers grown under low As/III ratio," Appl. Phys. Lett. **80**(14), 2445–2447 (2002).
3. N. Tansu and L. J. Mawst, "High-performance, strain compensated InGaAs-GaAsP-GaAs (λ=1.17 µm) quantum well diode lasers," IEEE Photon. Technol. Lett. **13**(3), 179–181 (2001).
4. N. Tansu, J. Y. Yeh, and L. J. Mawst, "High-performance 1200-nm InGaAs and 1300-nm InGaAsN quantum well lasers by metal–organic chemical vapor deposition," IEEE J. Sel. Top. Quantum Electron. **9**(5), 1220–1227 (2003).
5. N. Tansu, J.-Y. Yeh, and L. J. Mawst, "Physics and characteristics of high performance 1200 nm InGaAs and 1300–1400 nm InGaAsN quantum well lasers obtained by metal–organic chemical vapour deposition," J. Phys. Condens. Matter **16**(31), S3277–S3318 (2004).
6. V. Gambin, W. Ha, M. Wistey, H. Yuen, S. R. Bank, S. M. Kim, and J. S. Harris, "GaInNAsSb for 1.3-1.6-µm-long wavelength lasers grown by molecular beam epitaxy," IEEE J. Sel. Top. Quantum Electron. **8**(4), 795–800 (2002).
7. N. Tansu and L. J. Mawst, "Current injection efficiency of InGaAsN quantum-well lasers," J. Appl. Phys. **97**(5), 054502 (2005).
8. S. R. Bank, L. L. Goddard, M. A. Wistey, H. B. Yuen, and J. S. Harris, "On the temperature sensitivity of 1.5 µm GaInNAsSb lasers," IEEE J. Sel. Top. Quantum Electron. **11**(5), 1089–1098 (2005).
9. I. Vurgaftman, J. R. Meyer, N. Tansu, and L. J. Mawst, "(In) GaAsN-based type-II 'W' quantum-well lasers for emission at λ = 1.55 µm," Appl. Phys. Lett. **83**(14), 2742–2744 (2003).
10. N. Tansu and L. J. Mawst, "Design analysis of 1550-nm GaAsSb-(In)GaAsN type-II quantum well laser active regions," IEEE J. Quantum Electron. **39**(10), 1205–1210 (2003).
11. L. L. Goddard, S. R. Bank, M. A. Wistey, H. B. Yuen, Z. Rao, and J. S. Harris, "Recombination, gain, band structure, efficiency, and reliability of 1.5-µm GaInNAsSb/GaAs lasers," J. Appl. Phys. **97**(8), 083101 (2005).
12. M. Fallahi, L. Fan, Y. Kaneda, C. Hessenius, J. Hader, H. Li, J. V. Moloney, B. Kunert, W. Stolz, S. W. Koch, J. Murray, and R. Bedford, "5-W yellow laser by intracavity frequency doubling of high-power vertical-external-cavity surface-emitting laser," IEEE Photon. Technol. Lett. **20**(20), 1700–1702 (2008).
13. M. Jansen, G. P. Carey, R. Carico, R. Dato, A. M. Earman, M. J. Finander, G. Giaretta, S. Hallstein, H. Hofler, C. P. Kocot, S. Lim, J. Krueger, A. Mooradian, G. Niven, Y. Okuno, F. G. Patterson, A. Tandon, and A. Umbrasas, "Visible laser sources for projection displays," Proc. SPIE **6489**, 648908 (2007).
14. A. V. Shchegrov, J. P. Watson, D. Lee, A. Umbrasas, S. Hallstein, G. P. Carey, W. R. Hitchens, K. Scholz, B. D. Cantos, G. Niven, M. Jansen, J.-M. Pelaprat, and A. Mooradian, "Development of compact blue-green lasers for projection display based on Novalux extended-cavity surface-emitting laser technology," Proc. SPIE **5737**, 113–119 (2005).
15. L. F. Johnson, H. J. Guggenheim, T. C. Rich, and F. W. Ostermayer, "Infrared-to-visible conversion by rare-earth ions in crystals," J. Appl. Phys. **43**(3), 1125–1137 (1972).

16. F. Vetrone and J. A. Capobianco, "Lanthanide-doped fluoride nanoparticles: luminescence, upconversion, and biological applications," Int. J. Nanotechnol. **5**(9/10/11/12), 1306–1339 (2008).
17. C. Cao, W. Qin, J. Zhang, J. Zhang, Y. Wang, Y. Jin, G. Wei, G. Wang, and L. Wang, "Multicolor up-conversion emission of $Tm^{3+}/Er^{3+}/Yb^{3+}$ tri-doped YF_3 phosphors," J. Nanosci. Nanotechnol. **8**(3), 1384–1387 (2008).
18. M. Haase and H. Schäfer, "Upconverting nanoparticles," Angew. Chem. Int. Ed. Engl. **50**(26), 5808–5829 (2011).
19. F. Wang and X. Liu, "Recent advances in the chemistry of lanthanide-doped upconversion nanocrystals," Chem. Soc. Rev. **38**(4), 976–989 (2009).
20. C. Paßlick, B. Henke, I. Csaszar, B. Ahrens, P.-T. Miclea, J. A. Johnson, and S. Schweizer, "Advances in up- and down-converted fluorescence for high efficiency solar cells using rare-earth doped fluorozirconate-based glasses and glass ceramics," Proc. SPIE **7772**, 77720A (2010).
21. C. Mi, J. Zhang, H. Gao, X. Wu, M. Wang, Y. Wu, Y. Di, Z. Xu, C. Mao, and S. Xu, "Multifunctional nanocomposites of superparamagnetic (Fe_3O_4) and NIR-responsive rare earth-doped up-conversion fluorescent ($NaYF_4$: Yb,Er) nanoparticles and their applications in biolabeling and fluorescent imaging of cancer cells," Nanoscale **2**(7), 1141–1148 (2010).
22. A. Chavez-Pirson, "Highly doped phosphate glass fibers for fiber lasers and amplifiers with applications," Proc. SPIE **7839**, 78390K (2010).
23. M. Quintanilla, N. O. Núñez, E. Cantelar, M. Ocaña, and F. Cussó, "Tuning from blue to magenta the up-converted emissions of YF_3:Tm^{3+}/Yb^{3+} nanocrystals," Nanoscale **3**(3), 1046–1052 (2011).
24. D. K. Chatterjee, M. K. Gnanasammandhan, and Y. Zhang, "Small upconverting fluorescent nanoparticles for biomedical applications," Small **6**(24), 2781–2795 (2010).
25. J. Zhou, Z. Liu, and F. Li, "Upconversion nanophosphors for small-animal imaging," Chem. Soc. Rev. **41**(3), 1323–1349 (2012).
26. E. Cantelar, J. A. Muñoz, J. A. Sanz-Garcia, and F. Cusso, "Yb^{3+} to Er^{3+} energy transfer in $LiNbO_3$," J. Phys. Condens. Matter **10**(39), 8893–8903 (1998).
27. F. Auzel, "Upconversion and anti-Stokes processes with f and d ions in solids," Chem. Rev. **104**(1), 139–174 (2004).
28. J. F. Suyver, A. Aebischer, D. Biner, P. Gerner, J. Grimm, S. Heer, K. W. Krämer, C. Reinhard, and H. U. Güdel, "Novel materials doped with trivalent lanthanides and transition metal ions showing near-infrared to visible photon upconversion," Opt. Mater. **27**(6), 1111–1130 (2005).
29. G. Y. Chen, Y. Liu, Y. G. Zhang, G. Somesfalean, Z. G. Zhang, Q. Sun, and F. P. Wang, "Bright white upconversion luminesence in rare-earth-ion-doped Y_2O_3 nanocrystals," Appl. Phys. Lett. **91**(13), 133103 (2007).
30. F. Wang, Y. Han, C. S. Lim, Y. Lu, J. Wang, J. Xu, H. Chen, C. Zhang, M. Hong, and X. Liu, "Simultaneous phase and size control of upconversion nanocrystals through lanthanide doping," Nature **463**(7284), 1061–1065 (2010).
31. T. Passuello, F. Piccinelli, M. Pedroni, M. Bettinelli, F. Mangiarini, R. Naccache, F. Vetrone, J. A. Capobianco, and A. Speghini, "White light upconversion of nanocrystalline Er/Tm/Yb doped tetragonal $Gd_4O_3F_6$," Opt. Mater. **33**(4), 643–646 (2011).
32. Q. Lü, Y. Wu, A. Li, Y. Wang, Y. Gao, and H. Peng, "Local thermal effect at luminescent spot on upconversion luminescence in Y_2O_3:Er^{3+}, Yb^{3+} nanoparticles," Mater. Sci. Eng. B **176**(14), 1041–1046 (2011).
33. A. M. Barnett, "Seeing, red, yellow and green in a semiconductor alfanumeric display," Electronics **43**(10), 88–93 (1970).
34. H. Naruke, T. Mori, and T. Yamase, "Luminescence properties and excitation process of a near-infrared to visible up-conversion color-tunable phosphor," Opt. Mater. **31**(10), 1483–1487 (2009).
35. A. Rapaport, J. Milliez, M. Bass, A. Cassanho, and H. Jenssen, "Role of pump duration on temperature and efficiency of up-conversion in fluoride crystals co-doped with ytterbium and thulium," Opt. Express **12**(21), 5215–5220 (2004).
36. E. Cantelar, R. Nevado, G. Lifante, and F. Cusso, "Modelling of optical amplification in Er/Yb co-doped $LiNbO_3$ waveguides," Opt. Quantum Electron. **32**(6-8), 819–827 (2000).
37. L. Nuñez, G. Lifante, and F. Cusso, "Polarization effects on the line-strength calculations of Er^{3+}-doped $LiNbO_3$," Appl. Phys. B **62**(5), 485–491 (1996).
38. E. Cantelar, R. E. Di Paolo, F. Cusso, R. Nevado, G. Lifante, W. Sohler, and H. Suche, "Spectroscopy of Er^{3+} in Zn-diffused $LiNbO_3$ waveguides," J. Alloy. Comp. **323–324**, 348–350 (2001).
39. M. Ramirez, M. L. Bausa, S. W. Biernacki, A. Kaminska, A. Suchocki, and M. Grinberg, "Influence of hydrostatic pressure on radiative transition probability of the intrashell 4f transitions in Yb^{3+} ions in lithium niobate crystals," Phys. Rev. B **72**(22), 224104 (2005).
40. E. Cantelar and F. Cusso, "Competitive up-conversion mechanisms in Er^{3+}/Yb^{3+} co-doped $LiNbO_3$," J. Lumin. **102–103**, 525–531 (2003).
41. M. Pollnau, D. R. Gamelin, S. R. Luthi, H. U. Gudel, and M. P. Hehlen, "Power dependence of upconversion luminescence in lanthanide and transition-metal-ion systems," Phys. Rev. B **61**(5), 3337–3346 (2000).
42. B. Simondi-Teisseire, B. Viana, D. Vivien, and A. M. Lejus, "Yb^{3+} to Er^{3+} energy transfer and rate-equations formalism in the eye safe laser material Yb:Er:$Ca_2Al_2SiO_7$," Opt. Mater. **6**(4), 267–274 (1996).
43. D. L. Veasey, J. M. Gary, J. Amin, and J. A. Aust, "Time-dependent modelling of erbium-doped waveguide lasers in lithium niobate pumped at 980 and 1480nm," IEEE J. Quantum Electron. **33**(10), 1647–1662 (1997).
44. V. Dierolf, A. B. Kutsenko, C. Sandmann, F. Tallian, and A. N. D. W. Von Der Osten, "Towards new lasers in Ti:ER:$LiNbO_3$ waveguides: a study of the excited ER^{3+} states," Appl. Phys. B **68**(5), 767–775 (1999).
45. J. C. Boyer, L. A. Cuccia, and J. A. Capobianco, "Synthesis of colloidal upconverting $NaYF_4$:Er^{3+}/Yb^{3+} and Tm^{3+}/Yb^{3+} monodisperse nanocrystals," Nano Lett. **7**(3), 847–852 (2007).

46. N. Nuñez, M. Quintanilla, E. Cantelar, F. Cusso, and M. Ocaña, "Uniform YF_3:Yb,Er up-conversion nanophosphors of various morphologies synthesized in polyol media through an ionic liquid," J. Nanopart. Res. **12**(7), 2553–2565 (2010).
47. Q. Lü, Y. J. Wu, A. H. Li, Y. Wang, Y. Gao, and H. Y. Peng, "Local thermal effect at luminescent spot on upconversion luminescence in Y_2O_3:Er^{3+},Yb^{3+} nanoparticles," Mater. Sci. Eng. B **176**(14), 1041–1046 (2011).
48. J. Zhang, Y. Wang, L. Guo, F. Zhang, Y. Wen, B. Liu, and Y. Huang, "Vacuum ultraviolet and near-infrared excited luminescence properties of $Ca_3(PO_4)_2$:RE^{3+}, Na^+ (RE=Tb, Yb, Er, Tm, and Ho)," J. Solid State Chem. **184**(8), 2178–2183 (2011).

1. Introduction

The pursuit of infrared-to-visible up-conversion method to achieve visible light emitters was strongly driven by the availability of high-performance and compact laser devices emitting in the infrared spectral regimes specifically covering from ~980 nm up to ~1400 nm [1–11]. These high performance IR lasers had been realized by using InGaAs quantum wells [1–3], InGaAsN quantum wells [4–7], and mixed Sb-N based quantum wells [8–11], resulting in very low threshold current density and high output power laser devices. These compact and low-cost IR diode lasers [1–11], which are useful as excitation pumps in up-conversion method, lead to strong motivation for development of various up-conversion methods for realizing practical visible light emitters [12–14]. The use of these IR diode lasers had also been used for achieving up-conversion via second harmonic generation [12–14], resulting in red / green / blue emitters applicable for laser TV and display technologies [12–14].

In addition, the availability of such high performance IR diode lasers for pumping rare-earth doped materials has also driven renewed interest in the preparation of new materials and novel applications which include displays, lasers and amplifiers, optical temperature sensors, biological markers and multiphotonic microscopy [15–23]. Particularly interesting at the moment is the development of materials with multiple emissions, suitable as biological markers and the control of their chromaticity [16,18,24,25].

Er^{3+}/Yb^{3+} co-doped materials have attracted particular attention in these applications because of the high absorption cross section of Ytterbium ions at 980 nm, a wavelength readily available with commercial semiconductor diode lasers, together with the efficient Yb^{3+} → Er^{3+} resonant energy transfer and the subsequent up-conversion processes leading to visible emissions [26–28].

Generally, there is the possibility of chromaticity modification through the choice of host and of dopant concentrations, that is, through the synthesis of different phosphors [29–32]. Also, there is an additional possibility of chromaticity tuning within a given phosphor with its given host and concentration of dopants, which relies on the dynamical dependence of the up-conversion processes on the duration of the excitation. This idea of tunable phosphors, which may be traced back to the early times of semiconductor design [33], has been revisited recently in other Yb^{3+} activated materials [34,35]. Nevertheless, the description of this phenomenon is so far mostly qualitative, lacking a quantitative treatment based on the dynamics of the luminescence and energy-transfer processes involved therein.

In order to understand the origin and the relevance of the different parameters involved in this phenomenon, here we present a study of the dynamics of the $LiNbO_3$: Er^{3+}/Yb^{3+} system under 980 nm modulated pumping. The advantage of this material, in addition to its applications in optoelectronic and integrated optics devices, lies in its well-known spectroscopic parameters [26,36–40], allowing a detailed analysis of the up-conversion dynamics.

2. Experimental system

Monocrystalline $LiNbO_3$: Er^{3+}/Yb^{3+} was grown by the Czochralski method with automatic diameter control by a crucible weighting system. The starting materials were congruent $LiNbO_3$ ([Li]/[Nb] = 0.945) and Erbium and Ytterbium oxides with a purity grade of 99.99%. The Er^{3+} and Yb^{3+} concentrations in the crystal (determined by an X-Ray Fluorescence Technique) were found to be 0.7 and 2.7 mol%, respectively (further details can be obtained

from the supplementary information attached to Fig. 1 (Media 1)). Z-cut slices of 1 mm width were cut and polished up to optical grade.

Photoluminescence experiments were performed by using a 980 nm laser diode (LIMO FQ-A0063), allowing the generation of symmetric square pulses. The luminescence signal was dispersed by a SpectraPro 500-i monocromator and detected by a Thorn Emi photomultiplier, QB9558 model. The signal was averaged by using a Keithley 6514 system electrometer and/or a TEKTRONIX TDS 420 oscilloscope.

3. Results and discussion

3.1 Emission spectroscopy

It is well known that the 980 nm pumping scheme in Er^{3+}/Yb^{3+} codoped materials gives rise to two intense visible emission bands in the green and red spectral ranges, associated to the $^2H_{11/2}$:$^4S_{3/2} \rightarrow {}^4I_{15/2}$ and $^4F_{9/2} \rightarrow {}^4I_{15/2}$ Er^{3+} transitions respectively [15]. Figure 1 shows the up-converted emission spectra (normalized to the red emission band) measured in the Er^{3+}/Yb^{3+}co-doped $LiNbO_3$ sample, after 980 nm pumping, for two symmetric square pulses of different width (1 ms, dotted black line; 60 ms, continuous red line). As can be seen, the relative intensity of green and red emissions depends on the frequency used to modulate the excitation beam, similarly to previous reports for other Er^{3+}/Yb^{3+} co-doped materials [34].
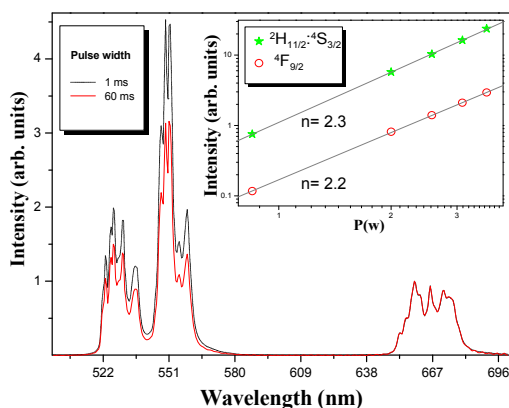

Fig. 1. A comparison of two emission spectra measured using symmetric square pulses of different width: 1 ms (black dotted line) and 60 ms (red solid line) width. The inset shows the power dependence of both emission bands, presented in double logarithmic representation (Media 1).

The inset of Fig. 1 shows the power dependence of the green and red up-converted emissions (in double-logarithmic scale). It is well known [41] that the intensity of up-converted luminescence I_{UC} depends on pump power P as $I_{UC} \propto P^n$, where n represents the number of photons absorbed in the process. It can be observed that, within the experimental error, both emissions exhibit a quadratic dependence (slope value close to n ≈2) indicating that the IR-to visible energy conversion operates by two-photon processes.

The dependences of green and red emissions on excitation modulation are presented in Fig. 2, where the overall intensities (measured as the area under the emission band) are represented as function of the excitation pulse width. It can be observed that both emissions increase monotonously for short modulation periods, reaching a plateau when the excitation window is sufficiently long. A closer look reveals a faster growth of the green emission, which reaches the saturation plateau before (i.e., at shorter widths than) the red emission. This is a clear indication that the dynamics of up-conversion processes leading to the green and red emissions are different, as shall next be examined in detail.
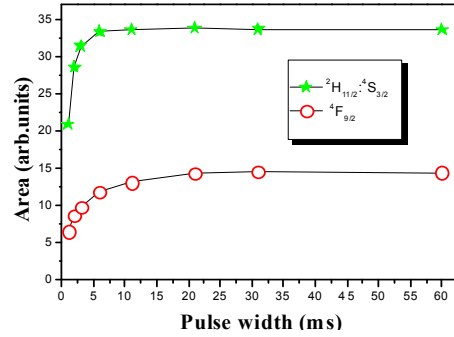
Fig. 2. Green ($^2H_{11/2}$:$^4S_{3/2} \rightarrow$ $^4I_{15/2}$) and red ($^4F_{9/2} \rightarrow$ $^4I_{15/2}$) emission areas as a function of the excitation pulse width.

3.2 Population dynamics

The effect of the excitation modulation on the up-conversion properties can be examined considering the different population paths involved in the generation of green and red emissions.

Er^{3+} green emissions arise from the $^2H_{11/2}$:$^4S_{3/2} \rightarrow$$^4I_{15/2}$ transition, and the energy transfer up-conversion processes that populate the emitting levels are depicted in Fig. 3(a). A first resonant energy transfer process that can operate forwards and backwards $^2F_{5/2} \leftrightarrow$ $^2F_{7/2}$ (Yb^{3+}):$^4I_{15/2} \leftrightarrow$ $^4I_{11/2}$ (Er^{3+}), populates the $^4I_{11/2}$ intermediate Er^{3+} level. A second resonant cross-relaxation from $Yb^{3+} \rightarrow Er^{3+}$ ($^2F_{5/2} \rightarrow$ $^2F_{7/2}$ (Yb^{3+}):$^4I_{11/2} \rightarrow$ $^4F_{7/2}$ (Er^{3+})) excites the Er^{3+} ion to the $^4F_{7/2}$ upper mainfold, from where the $^2H_{11/2}$:$^4S_{3/2}$ thermally coupled manifolds are populated by multiphonon decay. Additionally, under 980 nm pumping, these levels are also populated by excited-state absorption (ESA) from the $^4I_{11/2}$ manifold ($^4I_{11/2} \rightarrow$ $^4F_{7/2}$ transition).
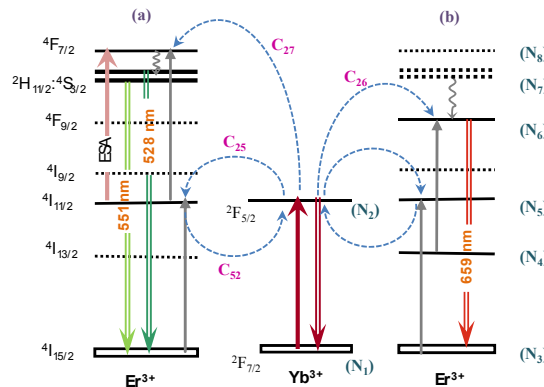

Fig. 3. Schematic diagram showing the processes involved in the population of the upper Er^{3+} manifolds responsible of the green (a) and red (b) emissions, after Yb^{3+} excitation at 980 nm.

On the other hand, the $^4F_{9/2}$ level responsible of the red emission ($^4F_{9/2} \rightarrow$ $^4I_{15/2}$), is populated partially by multiphonon relaxation from the upper $^2H_{11/2}$:$^4S_{3/2}$ manifolds, and also by an additional cross-relaxation mechanism ($^2F_{5/2} \rightarrow$ $^2F_{7/2}$ (Yb^{3+}):$^4I_{13/2} \rightarrow$ $^4F_{9/2}$ (Er^{3+})), now involving the long-lived $^4I_{13/2}$ Er^{3+} level, as sketched in Fig. 3(b).

The different lifetimes of the intermediate levels involved in those excitations are responsible for the different modulation-dependent up-conversion properties.

In order to further quantify the up-conversion temporal dynamics, we shall describe it by using the rate equations formalism [15,26,42] incorporating all the above mentioned processes. The temporal evolution of the population densities in the different manifolds is given by the following rate equations:

$$\frac{dN_7}{dt} = R_{57}N_5 + C_{27}N_2N_5 - \frac{N_7}{\tau_7} \qquad (1)$$

$$\frac{dN_6}{dt} = (A_{76} + W_{76}^{NR})N_7 + C_{26}N_2N_4 - \frac{N_6}{\tau_6} \qquad (2)$$

$$\frac{dN_5}{dt} = A_{75}N_7 + (A_{65} + W_{65}^{NR})N_6 + R_{35}N_3 + C_{25}N_2N_3 - C_{52}N_5N_1 - C_{27}N_2N_5 - (R_{57} + \frac{1}{\tau_5})N_5 \quad (3)$$

$$\frac{dN_4}{dt} = A_{74}N_7 + A_{64}N_6 + (A_{54} + W_{54}^{NR})N_5 - C_{26}N_2N_4 - \frac{N_4}{\tau_4} \qquad (4)$$

$$N_3 = N_{Er} - N_7 - N_6 - N_5 - N_4 \qquad (5)$$

$$\frac{dN_2}{dt} = R_{12}N_1 + C_{52}N_5N_1 - C_{25}N_2N_3 - C_{27}N_2N_5 - C_{26}N_2N_4 - \frac{N_2}{\tau_2} \qquad (6)$$

$$N_1 = N_{Yb} - N_2 \qquad (7)$$

where (N_i with $i = 1, 2, \ldots, 7$) represents the population densities in the corresponding levels, as indicated also in Fig. 3. A_{ij} and

$$W_{ij}^{NR} = \tau_i^{-1} - \sum_j A_{ij} \qquad (8)$$

represent the radiative and non-radiative transition probabilities respectively, associated to the $i \rightarrow j$ transition, τ_i being the experimental lifetime of the i-th level. C_{ij} are the macroscopic energy transfer coefficients. N_{Er} and N_{Yb} are total concentrations of erbium and ytterbium ions and, finally, the R_{mn} represents the pumping rates associated to the $m \rightarrow n$ transitions which are related to the corresponding absorption cross sections (σ_{mn}) by:

$$R_{mn}(\lambda) = \frac{\sigma_{mn}(\lambda)}{hc/\lambda} \times I_{exc} \qquad (9)$$

where I_{exc} stands for the excitation intensity. In Eqs. (1)–(7), energy transfer processes between Er^{3+} ions have not been included, given that their efficiencies are negligible compared to Yb^{3+} - Er^{3+} ion interactions [36]. All the spectroscopic parameters used in the model have been previously reported in the literature, and they are summarized in Table 1.

The population dynamics has been studied by integrating Eqs. (1)–(7) assuming that the excitation is modulated in the form of a square shaped pulse of constant amplitude and variable width, Λ (period $T = 2\Lambda$). Figure 4 represents the temporal evolution of the different population densities (N_i), calculated using a 4th-order Runge-Kutta algorithm, for three different pulse widths: $\Lambda = 300$ µs, $\Lambda = 3$ ms and $\Lambda = 30$ ms.

Figure 4(a) corresponds to the fastest modulation frequency or shortest pulse width: $\Lambda = 300$ µs. In this case the pulse width is shorter than the longest-lived Er^{3+} excited state, the metastable ${}^4I_{13/2}$ manifold ($\Lambda = 300$ µs $<< \tau_4 \approx 3$ ms), but comparable to or even longer than the natural lifetime of the other relevant Er^{3+} or Yb^{3+} excited states (see Table 1). Then, the excited states populations are driven by pump modulation which causes the levels to begin to fill up but stopping short of reaching their steady state populations. Also, when the excitation is removed, the system starts to decay, but only partially before a new pump cycle reinitiates the population increase. The fluctuations of these populations are clearly visible in the figure for all the excited states with the only exception of the metastable ${}^4I_{13/2}$ manifold, due to its much longer characteristic response time. Its population (N_4) grows almost steadily towards the saturation (steady state) value with much smaller fluctuations (barely visible in the figure).

Figure 4(c) corresponds to the opposite limit when modulating periods are much longer than the lifetimes of all manifolds, including the metastable one ($^4I_{13/2}$). In this case, the excitation period is long enough to allow all excited states to increase their population reaching the steady state (compare those values with the corresponding values of Fig. 4(a)). Also during the "dark period" the excited manifolds are given enough time to decay, losing practically all their population.
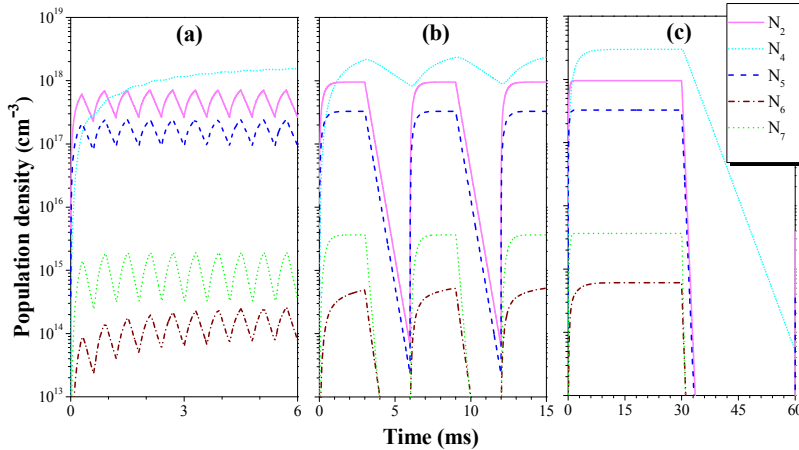

Fig. 4. Population dynamics calculated by numerical integration of Eqs. (1)-(7) with square pulse excitation of variable width: (a) 300 μs, (b) 3 ms and (c) 30 ms.

The more interesting case, Fig. 4(b), appears in between these two limits, when the excitation time is comparable with the longest lifetime of the system (Λ = 3 ms $\approx \tau_4$). In this temporal range, pump modulation results in a dissimilar behavior of long lived or short lived excited Er^{3+} levels. For instance, the $^2H_{11/2}$:$^4S_{3/2}$ manifolds, with a low lifetime value, have enough time to reach the steady state and therefore a constant population before the excitation turn-off occurs. In contrast, the $^4I_{13/2}$ and $^4F_{9/2}$ levels, whose temporal behavior is coupled via the non-resonant energy transfer mechanism $^2F_{5/2} \rightarrow {}^2F_{7/2}$ (Yb^{3+}):$^4I_{13/2} \rightarrow {}^4F_{9/2}$ (Er^{3+}), cannot achieve constant populations during the excitation window. Therefore, green and red Er^{3+} emissions, that originate from the $^2H_{11/2}$:$^4S_{3/2}$ and $^4F_{9/2}$ manifolds respectively, behave differently under modulated excitation and their intensity ratio can be controlled by changing the excitation pulse width. These differences can be experimentally verified, measuring luminescence intensities under modulated excitation. Figure 5 presents the temporal evolution of green and red emissions, normalized to their maximum value, obtained for two different pulse widths: (a) Λ = 3 ms and (b) Λ = 20 ms. These two ranges correspond to similar situations to these sketched in Figs. 4(b) and 4(c) and confirm that in the last case both emitting levels reach their saturation value, while in the former case this happens only for the green emitting levels ($^2H_{11/2}$:$^4S_{3/2}$) but not for the red emitting manifold ($^4F_{9/2}$), and therefore the relative intensities change with time. The figure includes also (solid lines) the theoretical prediction obtained by integration of Eqs. (1)–(7), using the spectroscopic parameters listed in Table 1 with C_{26} as fitting parameter. The best fit was obtained for $C_{26} \approx 0.2 \times C_{27}$, a value of the same order of magnitude but higher than that reported in the literature [40]. This value is consistent with the expected concentration dependence of this transfer coefficient [40] and, in fact, the sensitivity of the fitting of the temporal evolution (Fig. 5) indicates that this is a good method for C_{26} quantification. It should be noted that the calculation reproduces as well the luminescence decay times of both emissions, as shown in the inset of Fig. 5(b).
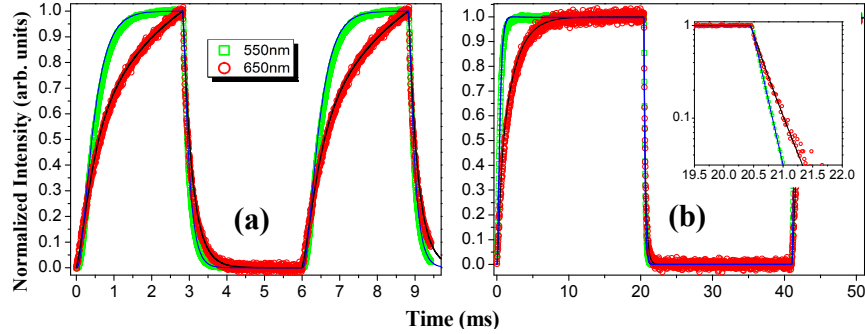
Fig. 5. Temporal evolution of the green and red luminescence, measured (symbols) and calculated (solid lines) for pulses of 3 ms and 20 ms width, (a) and (b) respectively.

Table 1. Spectroscopic Parameters of LiNbO$_3$:Er^{3+}/Yb^{3+}

Parameter	Value	Ref.
A_i		[37]
τ_2	370 µs	[39]
τ_4	2.7 ms	[38]
τ_5	220 µs	[37]
τ_6	1.6 µs	[37]
τ_7	25 µs	[37]
σ_{35} (980 nm)	5.50×10^{-21} cm^2	[43]
σ_{57} (980 nm)	3.50×10^{-21} cm^2	[44]
σ_{12} (980 nm)	2.10×10^{-20} cm^2	[36]
C_{25}	2.4×10^{-16} cm^3 s^{-1}	[26]
C_{52}	1.8×10^{-16} cm^3 s^{-1}	[26]
C_{27}	4.8×10^{-16} cm^3 s^{-1}	[26]
C_{26}/C_{27}	≈0.1	[40]
	≈0.2	Present work

3.3 "Green to Red Ratio"

As indicated above, the relative intensities of green and red emissions under modulated excitation depend on the excitation period. This can be quantified with the ratio between green and red emissions (*GRR*), which is presented in Fig. 6 as function of modulation frequency (*f* = 1/2*Λ*). The red symbols correspond to the experimental data for excitation pulses of between 1 ms and 100 ms width while the solid line represents the calculated values obtained by the rate equations model developed above. In the figure, for comparison purposes, the experimental and the calculated data were normalized to the *GRR* ratio for CW excitation (infinite pulse width).

For low modulation frequencies both green and red emitting levels reach their steady state population values and the luminescence behaves similarly to CW excitation, as expected. But increasing the modulation frequency, as indicated above, the intensity of the red emission starts to decrease, so that the relative green-to-red value increases. The dependence of *GRR* with modulation frequency (Fig. 6) presents a sigmoid shape (in semilogarithmic scale), reaching a saturation value when the pulse width approaches the longest lifetime of the system (a few milliseconds). It can be observed that the rate equations model correctly reproduces the experimentally observed modulation frequency dependence. This makes it possible to determine that the modulation frequency range where *GRR* can be modulated corresponds to frequencies slightly below the natural frequency of the longest-lived Er^{3+} level, that is, the metastable $^4I_{13/2}$ multiplet, which in LiNbO$_3$ corresponds to approximately 300 kHz.
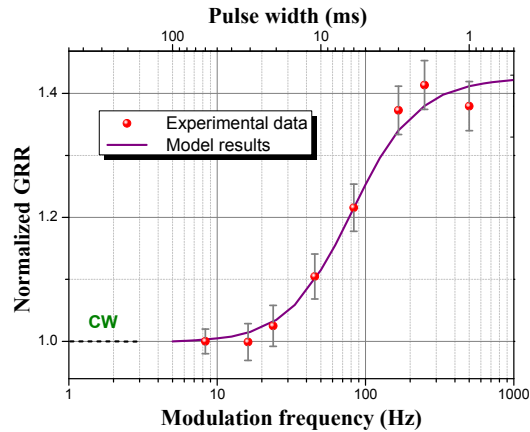
Fig. 6. Green to red ratio (GRR) as a function of the excitation pulse width.

The *GRR* value can be increased by a factor 1.4 in LiNbO$_3$ under modulation, although this figure is obviously dependent on the luminescence properties and spectroscopic characteristics of the material. In the case of LiNbO$_3$ where the green luminescence is dominant, such increase in *GRR* implies only a limited change in the chromaticity of the material which remains always within the 'green' region of the chromatic diagram. It seems plausible that in other hosts with stronger Erbium red emission, the increase of GRR with modulation might provide wider color tunability.

4. Conclusions

We may therefore conclude that LiNbO$_3$: Er^{3+}/Yb^{3+} system, emitting in green and red under Yb^{3+} pumping (around 980 nm), shows color-tunability under excitation modulation. This tunability arises from the different temporal response of the up-conversion processes that populate the green (^{2}H$_{11/2}$:^{4}S$_{3/2}$) and red (^{4}F$_{9/2}$) emitting levels. It is shown that modulation characteristics, including the GRR values, can be quantitatively explained by using the rate equations formalism. This formalism is adequate for any Er^{3+}/Yb^{3+} activated up-conversion phosphors and should be easily extended to other hosts, provided that the spectroscopic magnitudes that govern the emission dynamics are known. We have also identified the magnitudes needed in the rate equations model, and highlighted the fact that the modulation frequency range is governed by the natural lifetime of the metastable ^{4}I$_{13/2}$ Erbium level to a high extent.

Finally, it has also been demonstrated that the macroscopic transfer coefficient (C$_{26}$) that quantifies the efficiency of the cross-relaxation mechanism (^{2}F$_{5/2}$ $\rightarrow$ ^{2}F$_{7/2}$ (Yb^{3+}):^{4}I$_{13/2}$ $\rightarrow$ ^{4}F$_{9/2}$ (Er^{3+})), populating the ^{4}F$_{9/2}$ red-emitting Er^{3+} level, can be determined from the temporal evolution of the up-converted emissions, using the rate equations formalism.

Although the color modulation achievable in LiNbO$_3$: Er^{3+}/Yb^{3+} is limited (being in fact smaller than in other reported systems [34]), it is plausible to suppose that other hosts, with stronger red emission under CW pumping, could provide a wider modulation dependent color tunability. There are a number of Er^{3+}/Yb^{3+} doped materials where such intense red emission has been reported [45–48] and are therefore potential candidates for wide color tunability by excitation modulation.

Acknowledgments